1

Utilizing Phase Separation Reactions for Enhancement of the Thermoelectric Efficiency in IV–VI Alloys

Yaniv Gelbstein

Ben-Gurion University of the Negev, Department of Materials Engineering, Beer-Sheva, 84105, Israel
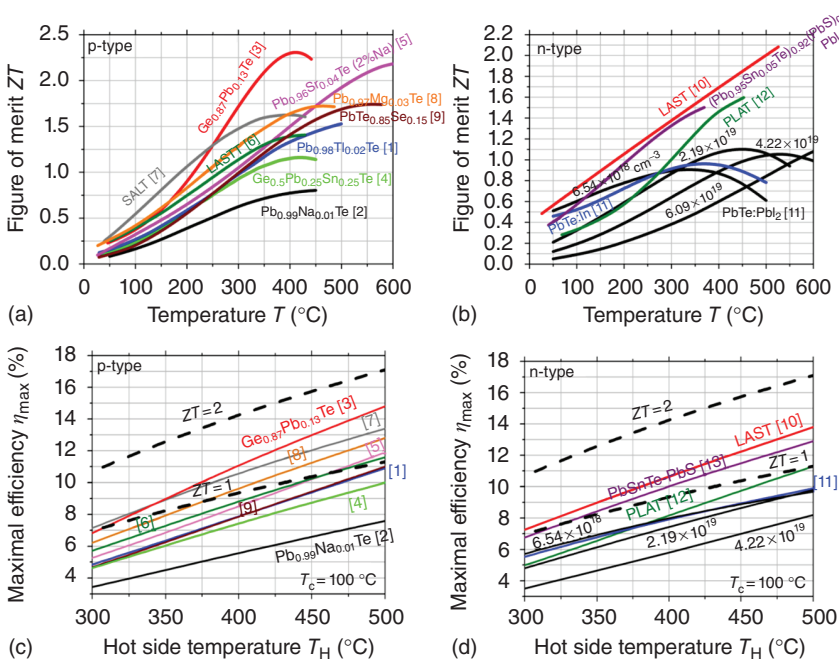
1.1 Introduction

In recent years, demands for energy efficiency have motivated many researchers worldwide to seek innovative methods capable of enhancing the efficiency of the thermoelectric energy conversion of heat to electricity. Since the dimensionless thermoelectric figure of merit ZT ($=\alpha^2\sigma T/\kappa$, where α is the Seebeck coefficient, σ is the electrical conductivity, κ is the thermal conductivity, and T is the absolute temperature) can be regarded to be proportional to the thermoelectric efficiency for a given temperature difference, materials improvements in this direction include either electronic optimization methods for maximizing the $\alpha^2\sigma$ product or phonons scattering methods for minimizing the thermal conductivity (the denominator of ZT). These methods and approaches mainly involve interfaces and submicron generation methods, which are much more effective in phonon scattering (rather than electron scattering), and consequently reducing the lattice contribution to the thermal conductivity, κ_L, without adversely affecting the other involved electronic properties. The main challenge while dealing with submicron features and interfaces for phonon scattering lies in the ability to retain these features under the thermal conditions involved and the suppression of undesirable coarsening effects over time. One plausible method for overcoming this challenge is based on using thermodynamically driven phase separation (i.e., spinodal decomposition or nucleation and growth) reactions, resulting in submicron and multiinterface features, owing to the separation of the matrix into two distinct phases, upon controlled heat treatments. The resultant features from these reactions are considered as more thermodynamically stable than other conventional nanostructuring methods, based on rapid consolidation of nanopowders obtained by energetic ball milling or melt spinning, which are susceptible to grain growth upon prolonged high temperature operation conditions. The key in choosing appropriate thermoelectric compositions, which follow phase separation reactions, is the requirement for a miscibility gap between the involved phases. This condition is strongly dependent on the nature

of the chemical pair interaction between the involved substitution elements. They can either distribute randomly in the host materials or separate the system into different phase components. An attractive chemical interaction can lead to an inhomogeneous distribution of the substitution atoms, leading to phase separation. Otherwise, the atoms will be substituted in the host system with a high solubility, forming a single solid solution phase. For achieving phase separation, compositions with attractive chemical interactions are required.

1.2 IV–VI Alloys for Waste Heat Thermoelectric Applications

The binary IV–VI compounds, based on columns IV (Ge, Pb, and Sn) and VI (Te, Se, and S) of the periodic table, are narrow-band ($\sim$0.2–0.3 eV) mixed ionic–covalent compounds, which are known for several decades as the most efficient thermoelectric materials for intermediate temperature ranges of up to 500 °C. The possibility for operation under the temperature range of 100–500 °C is significant from a practical point of view for converting waste heat generated in automotive diesel engines, in which a maximal temperature of 500 °C is developed, into useful electricity, and thus reducing fuel consumption and CO_2 emission. In the automotive industry, the minimal cold side temperature of $\sim$100 °C is mainly limited by the maximum available water flow rate through the radiator.

Lead chalcogenides (PbTe, PbSe, and PbS) crystallize in a NaCl cubic lattice, similarly to what happens in the high temperature phases of SnTe and GeTe. The latter follow a second-order lattice distortion to rhombohedral or orthorhombic structures upon decreasing the temperature, the significance of which on practical thermoelectric applications will be reviewed in detail in the following paragraphs. Another characteristic of the IV–VI compounds is the large deviation of stoichiometry, which in the case of PbTe is extended toward both Pb- and Te-rich compositions, enabling control of the electronic conduction toward n- and p-type conduction, respectively. In the case of GeTe, the deviation of stoichiometry is toward Te-rich compositions only, resulting in high carrier concentration (10^{20}–10^{21}/cm^3) p-type conduction, which is beyond the optimal required for thermoelectric applications ($\sim$$10^{19}$/cm^3). To reduce the holes concentration in order to obtain optimal thermoelectric properties, it is necessary to dope GeTe with donor-type electroactive impurities. Bi_2Te_3 acts as a donor when it is dissolved in GeTe. In the case of PbTe, the most common dopants are PbI_2 and Bi for obtaining optimal thermoelectric n-type compositions and Na for the p-type. Yet, for many years, owing to opposite influences of the carrier concentration on the various properties involved in the thermoelectric figure of merit, *ZT,* all the attempts to maximize the *ZT* value of the binary IV–VI compounds beyond $\sim$1 just by electronically doping optimization did not succeed. In the recent years, combined methods of electronic optimization and nanostructuring for reduction of the lattice thermal conductivity in IV–VI based alloys resulted in much higher *ZT* values of up to $\sim$2.2, as can be seen in Figure 1.1a,b for various p- and n-type compositions, respectively [1–13].

Figure 1.1 *ZT* values of the most efficient IV–VI alloys recently published – the p-type: $Pb_{0.98}Tl_{0.02}Te$ [1], $Pb_{0.99}Na_{0.01}Te$ [2], $Ge_{0.87}Pb_{0.13}Te$ [3], $Ge_{0.5}Pb_{0.25}Sn_{0.25}Te$ [4], $Pb_{0.96}Sr_{0.04}Te$ (2%Na) [5], $Ag_{0.9}Pb_5Sn_3Sb_{0.7}Te_{10}$ – LASTT [6], $Na_{0.95}Pb_{20}SbTe_{22}$ – SALT [7], $Pb_{0.97}Mg_{0.03}Te$:Na [8], $PbTe_{0.85}Se_{0.15}$:2%Na [9]; and n-type: $AgPb_{18}SbTe_{20}$ – LAST [10], PbTe (0.1 at%In) [11], PbI_2 doped PbTe with various carrier concentrations of 6.54×10^{18}, 2.19×10^{19}, 4.22×10^{19} and $6.09 \times 10^{19}/cm^3$ [11], $K_{0.95}Pb_{20}Sb_{1.2}Te_{22}$ – PLAT [12], and $(Pb_{0.95}Sn_{0.05}Te)_{0.92}(PbS)_{0.08}$:0.055 mol% PbI_2 [13]. (Pei *et al*. 2012 [8]. Reproduced with permission of Nature Publishing Group.)

It can be seen in the figure that early attempts to optimize the p-type Na-doped PbTe ($Pb_{0.99}Na_{0.01}Te$ [2]) and the n-type PbI_2-doped PbTe with various carrier concentrations of 6.54×10^{18}, 2.19×10^{19}, 4.22×10^{19}, and $6.09 \times 10^{19}/cm^3$ [11] resulted in relatively low maximal *ZT*s of 0.8 and 1.1, respectively. An effect of reduction of the carrier concentration on reduction of the maximal temperature at which maximal *ZT* is obtained because of electronic doping optimization can be easily seen for the PbI_2-doped PbTe [11] compositions in the figure. This finding had initiated the functionally graded materials (FGM) concept, in which thermoelectric legs composed of a singular matrix compound (e.g., PbTe) doped by a gradual dopant concentration, each optimal in its correspondent temperature along the leg, yield higher average *ZT* values than any singular doping concentration over the wide temperature gradients, usually apparent in practical operations. Yet, even this approach did not yield average *ZT*s higher than 1 for common operation conditions of 100–500 °C, and novel approaches for *ZT* enhancement had to be considered. One of such approaches, inspired by Kaidanov and Ravich [14], was based on advanced electronic doping based on generation of localized "deep" resonant states lying inside the energy gap, which are capable of pinning the Fermi energy of the compounds at a

favorable level, required for electronic thermoelectric optimization. Related to IV–VI based compounds, it was found that Group III dopants (Al, Ga, In, Tl) can be utilized for generation of such states. Application of this approach for thermoelectric optimization of n-type In-doped PbTe [11] resulted in higher average ZT for the temperature range of 100–500 than any of the PbI_2-doped materials, but without any success in increasing the average ZT beyond 1. On the other hand, a dramatic increase of the maximal ZT to a level of ~1.5 was recently demonstrated upon Tl doping of PbTe for the p-type $Pb_{0.98}Tl_{0.02}Te$ [1] composition (Figure 1.1a). A second approach that was taken in the recent years for enhancement of the ZT values of IV–VI based alloys is based on nanostructuring for reduction of the lattice thermal conductivity. Several examples of nanostructured materials with maximal ZTs higher than 1 and in some cases even higher than 2 are illustrated in Figure 1.1a,b. These include the p-type $Ag_x(Pb,Sn)_mSb_yTe_{2+m}$ (LASTT) [6], $NaPb_mSbTe_{2+m}$ (SALT) [7], $Ge_x(Sn_yPb_{1-y})_{1-x}Te$ [3, 4], and the n-type $AgPb_mSbTe_{2+m}$ (LAST) [10], KPb_mSbTe_{m+2} (PLAT) [12], and $(Pb_{0.95}Sn_{0.05}Te)_x(PbS)_{1-x}$ [13] families of materials; all exhibit nanostructures and very low lattice thermal conductivities. Different mechanisms for nanostructuring are involved in the above-listed examples. Yet, two of the most efficient materials listed in Figure 1.1a,b are the p-type $Ge_{0.87}Pb_{0.13}Te$ [3] and the n-type $(Pb_{0.95}Sn_{0.05}Te)_{0.92}(PbS)_{0.08}$ [13] compositions, both following thermodynamically driven phase separation reactions of the matrix into two distinct submicron phases. Since such reactions and the correspondent nanophases are considered as much more thermodynamically stable than many of the other methods listed above, as required for long-term thermoelectric applications, a detailed description of this effect and the conditions for achieving it will be given in the next paragraph.

It is noteworthy that the above-listed methods and compositions resulting in maximal ZTs higher than 1, as shown in Figure 1.1a,b, did not necessarily result in higher average ZTs than 1 over the entire operation temperature range (100–500 °C) required for automotive waste heat recovery. For such applications the maximal possible thermoelectric efficiency, defined as the ratio between the obtained electrical power on the load resistance and the absorbed heat, can be calculated using Eq. (1.1).

$$\eta = \frac{\Delta T}{T_H} \cdot \frac{\sqrt{1 + \overline{ZT}} - 1}{\sqrt{1 + \overline{ZT}} + \dfrac{T_C}{T_H}} \tag{1.1}$$

where η is the thermoelectric efficiency, $\overline{ZT}$ is the average dimensionless thermoelectric figure of merit, T_C is the cold side temperature of the thermoelectric sample, T_H is the hot side temperature of the thermoelectric sample, and ΔT is the temperature difference along the thermoelectric sample ($\Delta T = T_H - T_C$).
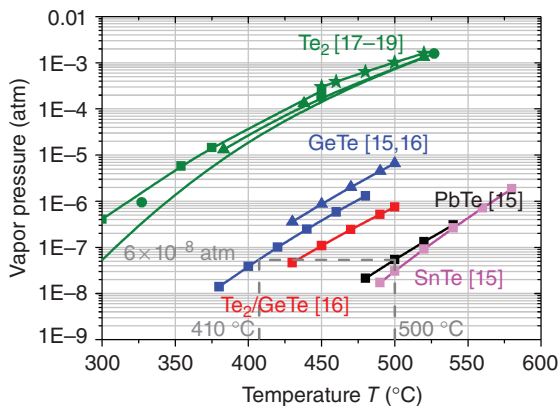
The maximal thermoelectric efficiency values for the samples shown in Figure 1.1a,b, calculated using Eq. (1.1) and the average ZTs for each composition, are illustrated in Figure 1.1c,d for a constant cold side temperature of 100 °C and varied hot side temperatures in the range of 300–500 °C. From these figures it can be easily seen that some of the recently published compositions

showing maximal ZTs higher than 1 and in some cases even higher than 1.6, do not necessarily show higher efficiency values than those calculated using Eq. (1.1) for an average ZT of 1 (dashed line in the figure). On the other hand, some of the compositions show very high efficiency values of up to 14–15% (the p-type $Ge_{0.87}Pb_{0.13}Te$ [3] and the n-type $AgPb_{18}SbTe_{20} - LAST$ [10] compositions) for the temperature range of 100–500 °C.

Besides high average ZTs, other important factors required for practical applications include high mechanical properties and improved structural and chemical stability at the operating temperatures. Mechanical properties are important in determining the performance of thermoelectric materials since they are subject in the course of their operation to various mechanical and thermal stresses. In this context, it was recently shown that the less thermo-electrically efficient p-$Pb_{1-x}Sn_xTe$ compound, compared to Na-doped PbTe, is more favorable for practical thermoelectric applications because of the highly mechanical brittle nature of the latter [2]. Regarding chemical and structural stability, PbTe-based compounds were associated for many years with improved structural and chemical stability at the operating temperatures than GeTe-based compounds. The improved chemical stability is due to a lower vapor pressure, namely, lower sublimation rates of PbTe, as can be seen in Figure 1.2.

In telluride-based thermoelectric materials (e.g., PbTe and GeTe), the main degradation mechanism during normal operation conditions (100–500 °C) is sublimation of GeTe, PbTe, or SnTe in a molecular form (Figure 1.2). For PbTe, the maximal allowed hot side temperature for long operation conditions is 500 °C, corresponding to a maximal vapor pressure of $\sim 6 \times 10^{-8}$ atm (Figure 1.2). It can be seen from the figure that this vapor pressure corresponds to a temperature of $\sim$410 °C for the case of GeTe, which can be considered as the maximal allowed operation temperature for this class of materials. Beyond this temperature, high sublimation and corresponding degradation rates can be expected. An improved structural stability of PbTe compared to GeTe was considered for many years mainly because of the single-phase cubic NaCl structure of PbTe over the whole operating temperature range, in contrast to the rhombohedral to cubic NaCl phase transition at 427 °C in GeTe. Recently, the highly efficient

Figure 1.2 Temperature dependence of the vapor pressures of various IV–VI alloys and the mostly volatile elements in these systems [15–19].

p-type $Ge_xPb_{1-x}Te$ alloys, including the $Ge_{0.87}Pb_{0.13}Te$ composition shown in Figure 1.1a, were shown to follow a second-order phase transition from the high-temperature cubic phase to the low-temperature rhomoboheral phase with a decreased phase transition temperature, T_c, by moving from GeTe toward PbTe richer compositions [20]. Second-order phase transitions occur when a new state of reduced symmetry develops continuously from the disordered (high temperature) phase and are characterized by the absence of discontinuities of the thermodynamic state functions (entropy, enthalpy, volume). The character of the phase transition (first- or second-order) is important to determine whether a certain material is suitable for serving in thermoelectric applications in which large temperature gradients are usually involved. In such instances, a singular intermediate temperature T_c at which one crystal structure is transformed into another with the corresponding sharp variation of the lattice parameters (as in first-order transitions) can result in mechanical weakness. A continuous variation of the lattice parameters from one phase to the other (as in second-order transitions) is more favorable from the mechanical stability standpoint. Therefore, $Ge_xPb_{1-x}Te$ alloys exhibit a very high potential, both from mechanical stability and thermoelectric performance considerations, for being involved as p-type legs in practical thermoelectric applications. Since the very high maximal ZTs of the p-type $Ge_{0.87}Pb_{0.13}Te$ and the n-type $(Pb_{0.95}Sn_{0.05}Te)_{0.92}(PbS)_{0.08}$ compositions in Figure 1.1a,b are mainly attributed to very low lattice thermal conductivity values resulting from nano- and submicron features originating from phase separation reactions, a detailed description of these reactions and their potential in enhancement of the thermoelectric figure of merit is given in the next paragraph.

1.3 Thermodynamically Driven Phase Separation Reactions

As mentioned earlier, retaining a submicron structure during a practical thermoelectric operation under a large temperature gradient is of great importance. One method for retaining such structures is based on the generation of thermodynamically driven phase separation reactions such as spinodal decomposition or nucleation and growth. For understanding the thermodynamic conditions required for generation of such reactions, a basic understanding of the thermodynamics of mixing is required and will be given referring to Figure 1.3.

The Gibbs energy of mixing, ΔG_m, for a binary A–B mixture, can be described in terms of Eq. (1.2) [21].

$$\Delta G_m = \Delta H_m - T\Delta S_m$$
$$= \omega \cdot x \cdot (1-x) + T \cdot R \cdot [(1-x) \cdot \ln(1-x) + x \cdot \ln(x)] \qquad (1.2)$$

The left term of Eq. (1.2) represents the enthalpy of mixing, ΔH_m, while the right term represents the entropy term of mixing $(-T\Delta S_m)$, where T is the absolute temperature, ΔS_m is the entropy of mixing, x is the concentration of one of the mixture's components (the concentration of the other component is therefore
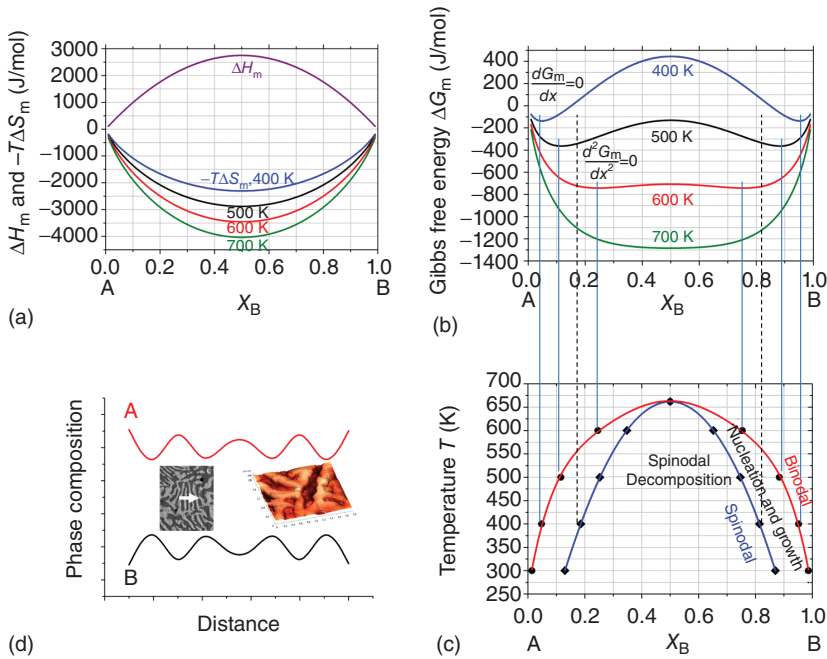
Figure 1.3 Compositional dependencies of the enthalpy, ΔH_m, entropy, $-T\Delta S_m$, terms of mixing (a), and Gibbs free energy of mixing, ΔG_m (b) for various temperatures; a phase diagram, built from the thermodynamic terms mentioned above, showing a miscibility gap between two components A and B in a binary mixture (c) and a representative phase separation microstructure showing a continuous variation of the concentration of the components A and B in the A–B binary mixture described above (d).

$1 - x$), ω is the interaction parameter between the mixture's components A and B, and R is the ideal gas constant ($=8.314$ J/mol/K). In ideal mixtures or ideal solutions, in which the enthalpies of mixing equal zero, ΔG_m is solely determined by the entropy of mixing. The regular solution model, described by Eq. (1.2), is a simple example of a nonideal solution that can be referred to many of the binary mixtures available in practical thermoelectric systems. ΔS_m is always positive, since there is always a positive entropy gain upon mixing, and therefore $-T\Delta S_m$ is always negative, as described in Figure 1.3a for various temperatures. Therefore, it can be shown that entropy considerations will solely lead to a homogeneous solution with an always negative ΔG_m function. Consequently, the miscibility characteristics of the two components A and B in a binary mixture are solely determined by the enthalpy of mixing and more specifically by the dimensionless interaction parameter ω (Eq. (1.2)) between the mixture's components. A negative chemical interaction ($\omega < 0$), which is the most common situation, will lead to a high solubility substitution of the matrix A and B atoms, forming a single solubility phase. In this case, both ΔH_m and ΔG_m will follow the same trend of the ($-T\Delta S_m$) function in Figure 1.3a, exhibiting one deep minimum. A more rare situation, in which an attractive chemical interaction

($\omega > 0$) exists, can lead to an inhomogeneous distribution of the substitution atoms, leading to phase separation and a miscibility gap in the phase diagram as will be explained in the following few sentences. In this case, ΔH_m will follow the trend observed in Figure 1.3a, exhibiting one maximum, and ΔG_m, which is the sum of the positive ΔH_m and the negative ($-T\Delta S_m$) functions, and will follow the two local minima trend shown in Figure 1.3b. The ΔG_m curves, obtained at various temperatures as shown in Figure 1.3b, can determine the phase diagram of the system (Figure 1.3c). Steady-state conditions, defined by the binodal curve, representing the limits of solid solubility, can be obtained by the intersection of each of the isothermal curves of Figure 1.3b with a common tangent. These are the local minima compositions, obtained for each temperature, satisfying the $dG_m/dx = 0$ condition. The spinodal curve of the phase diagram (Figure 1.3c) is determined by the inflection points ($d^2G_m/dx^2 = 0$) of the free energy isotherms of Figure 1.3b. Under the spinodal curve, namely, between the inflection points, where the curvature of the free energy function is negative ($d^2G_m/dx^2 < 0$), the spinodal decomposition mechanism of phase separation can occur. Therefore, for compositions within the spinodal curve, a homogeneous solution is unstable against microscopic compositional fluctuations, and there is no thermodynamic barrier to the growth of a new phase. As a result, the phase transformation is spontaneous, does not require any external activation energy, and is solely diffusion controlled. The compositions between the spinodal and the binodal curves, in which the curvature of the free energy function is positive ($d^2G_m/dx^2 > 0$), are considered as metastable, and in this region of the phase diagram the nucleation and growth mechanism for phase separation will dominate. In this region, a nucleus of a critical size has to form before it is energetically favorable for it to grow. Therefore, in contrast to the spinodal decomposition which can be treated purely as a diffusion problem, by an approximate analytical solution to the general diffusion equation, theories of nucleation and growth have to involve thermodynamic considerations, and the diffusion problem involved in the growth of the nucleus is far more difficult to solve. Furthermore, owing to the rapid phase separation mechanism involved in spinodal decomposition, this reaction is uniformly distributed throughout the materials by continuous low amplitude periodic modulations and not just at discrete nucleation sites as in the nucleation and growth regime. As a result, spinodal decomposition is characterized by a very finely dispersed microstructure, shown in Figure 1.3d, which can significantly reduce the lattice thermal conductivity and consequently maximize *ZT*. In this figure, the continuous compositional modulations of A and B atoms, obtained by crossing the two separated phases, can be easily seen. The first explanation of the fluctuation's periodicity was originally given by Hillert [22], upon derivation of a flux equation for one-dimensional diffusion on a discrete lattice based on a regular solution model. The equation takes into account the interfacial energy effects between adjacent separated phases. Subsequently, the effects of coherency strains on dictating the morphology were included by Cahn [23]. Therefore, both of the phase separation phenomena described above represent two mechanisms by which a solution of two or more components can be separated into distinct phases with different chemical compositions and physical properties. Owing to the rapid reactions involved,

usually the associated microstructure is finely dispersed and in many cases under defined stabilization conditions as in the submicron range, which is optimal for reduction of the lattice thermal conductivity and enhancement of *ZT*. In recent years, several thermoelectric material classes have shown *ZT* enhancement due to phase separation of one single matrix composition into two distinct phases. One example is the Heusler family of compounds. Phase separation of the quaternary Heusler compounds $Co_2Mn_{1-x}Ti_xSn$ into Co_2MnSn and Co_2TiSn [24], and of $Ti_{(1-x)}Mn_xCoSb$ into $TiCoSb$ and $MnCoSb$ [25], resulting in submicron periodicity of the phase-separated material as well as a major reduction of the thermal conductivity was recently shown by Felser's group [24, 25]. Moreover, theoretical phase diagram calculations for the system $CoTi_{1-x}Fe_xSb$ clearly show a miscibility gap and a tendency for spinodal decomposition [26], highlighting the potential for enhancement of the *ZT* values due to phase separation in this system as well. In the next paragraph, several specific examples for IV–VI based compounds, exhibiting enhanced thermoelectric properties following phase separation reactions, will be given in more details.

1.4 Selected IV–VI Systems with Enhanced Thermoelectric Properties Following Phase Separation Reactions

As mentioned above in relation to Figure 1.1, two of the recently reported most efficient n- and p-type IV–IV based compounds are the $(Pb_{0.95}Sn_{0.05}Te)_{0.92}(PbS)_{0.08}$ and $Ge_{0.87}Pb_{0.13}Te$ compositions, respectively, both following a phase separation reaction into nanoscaled domains. Investigation of the quasi-binary PbTe–PbS and PbTe–GeTe phase diagrams (Figure 1.4a,b) reveals that both exhibit an extended miscibility gap and that both of the compositions mentioned above fall inside the nucleation and growth zone of the phase diagrams, namely, between the binodal and spinodal curves. It is noteworthy that for the former, the phase diagram of the $Pb_{0.95}Sn_{0.05}Te$–PbS system is also shown as a blue curve in the same graph, based on calculation of $Pb_{0.95}Sn_{0.05}Te$ using the PbTe–SnTe phase diagram instead of pure PbTe for the 100% point, pure PbS for the 0% point, and intermediate reported points at 900, 1000, and 1200 K [27]. Indeed, for $Ge_{0.87}Pb_{0.13}Te$, following a solution annealing treatment for stabilizing the matrix high temperature single phase at a high temperature (873 K), a series of lower temperature (723 K) aging thermal treatments resulted in nucleation of Pb- and Ge-rich domains [3] and corresponding low thermal conductivity values. In this case, the phases' stability over time was relatively high.

Another example of interest, concerning the $Ge_x(Sn_yPb_{1-y})_{1-x}Te$ compositions [4], is described in the following related to Figure 1.5. These compositions based on the quasi-ternary GeTe—PbTe—SnTe system include the specific p-type $Ge_{0.5}Pb_{0.25}Sn_{0.25}Te$ composition, exhibiting a maximal *ZT* of 1.2 as shown in Figure 1.1a and the widely investigated $Ge_{0.6}Sn_{0.1}Pb_{0.3}Te$ composition [29–32], the microstructure of which is shown in Figure 1.3d.

The GeTe—PbTe—SnTe quasi-ternary phase diagram, showing an extended miscibility gap and a tendency to phase separation, is illustrated in Figure 1.5a,

(a)

(b)
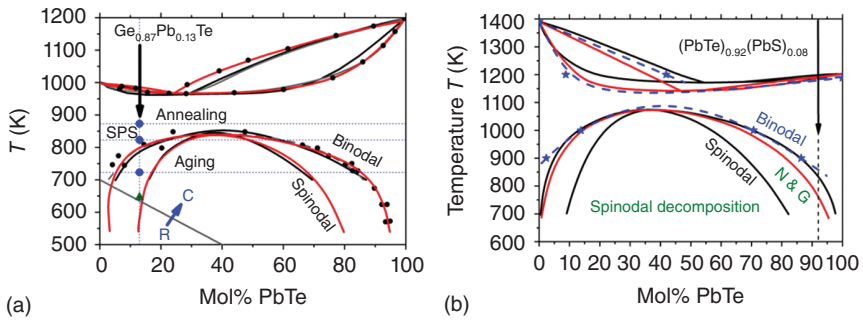
Figure 1.4 Quasi-binary PbTe—GeTe (a) [3] and PbTe—PbS (black curve [27], red curve [28], and blue curve – calculated for 100% Pb0.95Sn0.05Te instead of PbTe based on the PbTe—SnTe phase diagram [27]) and (b) phase diagrams showing a miscibility gap and a tendency for phase separation. The highly efficient $(Pb_{0.95}Sn_{0.05}Te)_{0.92}(PbS)_{0.08}$ and $Ge_{0.87}Pb_{0.13}Te$ thermoelectric compositions are clearly indicated. For the PbTe—GeTe phase diagram the transition temperatures from rhombohedral (R) to cubic (C) structures are also indicated. (Volykhov *et al*. 2006 [27]. Reproduced with permission of Springer.)

(a)

(b)

(c)

(d)
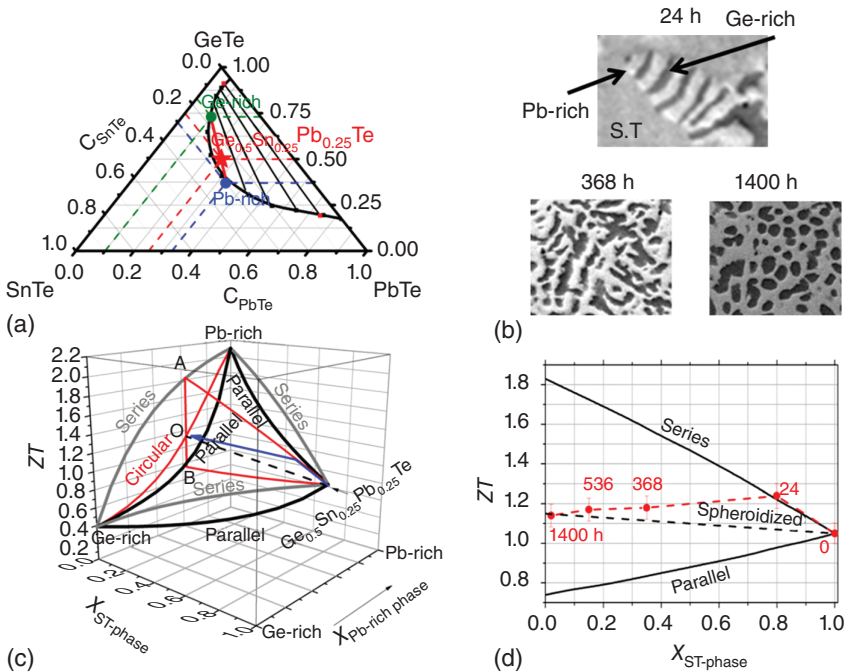
Figure 1.5 Quasi-ternary GeTe—PbTe—SnTe phase diagram showing a well-defined miscibility gap (a), as well as morphological (b), 3-D *ZT* (c), and 2-D *ZT* (d) variations upon thermal treatment at 400 °C for different durations for the p-type Ge0.5Pb0.25Sn0.25Te composition. (Gelbstein 2012 [4]. Reproduced with permission of Elsevier.)

indicating the nominal $Ge_{0.5}Pb_{0.25}Sn_{0.25}Te$ composition mentioned above, falling well inside the miscibility gap in the area corresponding to spinodal decomposition, which separates into Ge-rich (dark) and Pb-rich (bright) phases (Figure 1.5b). In this figure, it can be seen that the phase separation evolution follows various morphological stages from lamellar (at 24 h of 400 °C thermal treatment) to spheroidized (at 1400 h) geometries with some influence on the resultant ZT values as shown in Figure 1.5c,d. This figure shows results of the investigation of the influence of geometrical morphologies on ZT following various phase separation stages performed using the general effective media (GEM) theory [33], showing only slight variations of ZT during the phase separation reaction, highlighting the high thermoelectric stability of these reactions compared to other common nanogeneration methods.

1.5 Concluding Remarks

In the current chapter, the main advances in IV–VI based thermoelectric materials reported in recent years were reviewed. It was shown that during the recent years both due to nanostructuring methods for reduction of thermal conductivity and optimal electronic doping approaches, very high ZTs of up to ∼2.2 were achieved, rendering this class of thermoelectric materials as the most thermo-electrically efficient up to temperatures of ∼500 °C, which is ideal for converting the waste heat generated in diesel automotive engines into useful electricity. The generation of phase separation reactions for retaining the nanostructuring during practical operation conditions was described in detail as one of the most advanced approaches for ZT enhancement in such materials. The conditions for phase separation reactions, including the necessity for miscibility gap between the various components of the system and the distinction between the specific characteristics of the spinodal decomposition and nucleation and growth regimes of this gap, were described. Advanced optimal doping approaches based on generation of localized "deep" resonant states lying inside the energy gap, which are capable of pinning the Fermi energy of the compounds at a favorable level required for electronic thermoelectric optimization, were also described as useful for enhancement of the ZT values. All of the described methods for enhancing and retaining the ZT values upon long-term thermoelectric applications can be extended to many other classes of thermoelectric materials.

References

1 Heremans, J.P., Jovovic, V., Toberer, E.S., Saramat, A., Kurosaki, K., Charoenphakdee, A., Yamanaka, S., and Jeffrey Snyder, G. (2008) Enhancement of thermoelectric efficiency in PbTe by distortion of the electronic density of states. *Science*, **321**, 554–557.

2 Gelbstein, Y. (2011) $Pb_{1-x}Sn_xTe$ alloys: application considerations. *J. Electron. Mater.*, **40** (5), 533–536.

3 Gelbstein, Y., Davidow, J., Girard, S.N., Chung, D.Y., and Kanatzidis, M. (2013) Controlling metallurgical phase separation reactions of the $Ge_{0.87}Pb_{0.13}Te$ alloy for high thermoelectric performance. *Adv. Energy Mater.*, **3** (6), 815–820.

4 Gelbstein, Y. (2013) Phase morphology effects on the thermoelectric properties of $Pb_{0.25}Sn_{0.25}Ge_{0.5}Te$. *Acta Mater.*, **61**, 1499–1507.

5 Biswas, K., He, J., Blum, I.D., Wu, C.-I., Hogan, T.P., Seidman, D.N., Dravid, V.P., and Kanatzidis, M.G. (2012) High performance bulk thermoelectrics with all scale hierarchial architectures. *Nature*, **489**, 414–418.

6 Androulakis, J., Hsu, K.F., Pcionek, R., Kong, H., Uher, C., D'Angelo, J.J., Downey, A., Hogan, T., and Kanatzidis, M.G. (2006) Nanostructuring and high thermoelectric efficiency in *p*-Type $Ag(Pb_{1-y}Sn_y)_mSbTe_{2+m}$. *Adv. Mater.*, **18**, 1170–1173(LASTT).

7 Poudeu, P.F.P., D'Angelo, J., Downey, A.D., Short, J.L., Hogan, T.P., and Kanatzidis, M.G. (2006) High thermoelectric figure of merit and nanostructuring in bulk p-type $Na_{1-x}Pb_mSb_yTe_{m+2}$. *Angew. Chem. Int. Ed.*, **45**, 3835–3839(SALT).

8 Pei, Y., Wang, H., Gibbs, Z.M., LaLonde, A.D., and Jeffrey Snyder, G. (2012) Thermopower enhancement in $Pb_{1-x}Mn_xTe$ alloys and its effect on thermoelectric efficiency. *NPG Asia Mater.*, **4**, 1–6.

9 Pei, Y., Shi, X., LaLonde, A., Wang, H., Chen, L., and Jeffrey Snyder, G. (2011) Convergence of electronic bands for high performance bulk thermoelectrics. *Nature*, **473**, 66–69.

10 Hsu, K.F., Loo, S., Guo, F., Chen, W., Dyck, J.S., Uher, C., Hogan, T., Polychroniadis, E.K., and Kanatzidis, M.G. (2004) Cubic $AgPb_mSbTe_{2+m}$: bulk thermoelectric materials with high figure of merit. *Science*, **303**, 818.

11 Gelbstein, Y., Dashevsky, Z., and Dariel, M.P. (2005) High performance n-type PbTe-basedmaterials for thermoelectric applications. *Phys. B*, **363**, 196–205.

12 Poudeu, P.F.P., Gueguen, A., Wu, C.-I., Hogan, T., and Kanatzidis, M.G. (2010) High figure of merit in nanostructured n-type KPb_mSbTe_{m+2} thermoelectric materials. *Chem. Mater.*, **22**, 1046–1053.

13 Androulakis, J., Lin, C.-H., Kong, H.-J., Uher, C., Wu, C.-I., Hogan, T., Cook, B.A., Caillat, T., Paraskevopoulos, K.M., and Kanatzidis, M.G. (2007) Spinodal decomposition and nucleation and growth as a means to bulk nanostructured thermoelectrics: enhanced performance in $Pb_{1-x}Sn_xTe$–PbS. *J. Am. Chem. Soc.*, **129**, 9780–9788.

14 Kaidanov, V.I. and Ravich, Y.I. (1985) Deep and resonance states in $A^{IV} B^{VI}$ semiconductors. *Sov. Phys. Uspekhi*, **28** (1), 31–53.

15 Northrop, D.A. (1971) Thermogravimetric investigation of the vaporization of lead telluride, tin telluride, and germanium telluride. *J. Phys. Chem.*, **75** (1), 118.

16 Molchanov, M.V., Alikhanyan, A.S., Zlomanov, V.P., and Yashina, L.V. (2002) Mass spectrometric study of vapor composition over germanium telluride. *Inorg. Mater.*, **38** (6), 559.

17 Ubelis, A.P. (1982) Temperature dependence of the saturated vapor pressure of tellurium. *J. Eng. Phys. Thermophys.*, **42** (3), 309.

18 Dushman, S. (1962) *Scientific Foundations of Vacuum Technique*, 2nd edn, John Wiley & Sons, p. 669.

19 Madelung, O., Rössler, U., and Schulz, M. (eds) (1998) *Landolt–Bornstein-Group 3 Condensed Matter*, Non Tetrahedrally Based Elements and Binary Compounds I, vol. **41c**, Springer-Verlag, p. 1.

20 Gelbstein, Y., Ben-Yehuda, O., Dashevsky, Z., and Dariel, M.P. (2009) Phase transitions of p-type (Pb,Sn,Ge)Te based alloys for thermoelectric applications. *J. Cryst. Growth*, **311**, 4289–4292.

21 Ho, I.-H. and Stringfellow, G.B. (1996) Solid phase immiscibility in GaInN. *Appl. Phys. Lett.*, **69** (18), 2701–2703.

22 Hillert, M. (1961) A solid solution model for inhomogeneous systems. *Acta Metall.*, **9**, 525.

23 Cahn, W. (1961) On spinodal decomposition. *Acta Metall.*, **9**, 795.

24 Graf, T., Barth, J., Blum, C.G.F., Balke, B., and Felser, C. (2010) Phase-separation-induced changes in the magnetic and transport properties of the quaternary Heusler alloy $Co_2Mn_{1-x}Ti_xSn$. *Phys. Rev. B*, **82**, 104420.

25 Graf, T., Felser, C., and Parkin, S.S.P. (2011) Simple rules for the understanding of Heusler compounds. *Prog. Solid State Chem.*, **39**, 1–50.

26 Dinh, V.A., Sato, K., and Katayama-Yoshida, H. (2010) First principle study of spinodal decomposition thermodynamics in half-Heusler alloy $CoTi_{1-x}Fe_xSb$. *J. Superconduct. Novel Magnetis*, **23**, 75–78.

27 Volykhov, A.A., Yashina, L.V., and Shtanov, V.I. (2006) Phase relations in pseudobinary systems of germanium, tin, and lead chalcogenides. *Inorg. Mater.*, **42** (6), 596–604.

28 Laugier, A. (1973) Thermodynamics and phase diagram calculations in II–IV and IV–VI ternary systems using an associated solution model. *Rev. Phys. Appl.*, **8**, 259–269.

29 Gelbstein, Y., Dado, B., Ben-Yehuda, O., Sadia, Y., Dashevsky, Z., and Dariel, M.P. (2010) High thermoelectric figure of merit and nanostructuring in bulk p-type $Ge_x(Sn_yPb_{1-y})_{1-x}Te$ alloys following a spinodal decomposition reaction. *Chem. Mater.*, **22** (3), 1054–1058.

30 Dado, B., Gelbstein, Y., Mogilansky, D., Ezersky, V., and Dariel, M.P. (2010) The structural evolution following the spinodal decomposition of the pseudo-ternary $(Pb_{0.3}Sn_{0.1}Ge_{0.6})Te$ compound. *J. Electron. Mater.*, **39** (9), 2165–2171.

31 Dado, B., Gelbstein, Y., and Dariel, M.P. (2009) Nucleation of nano-size particles following the spinodal decomposition in the pseudo-ternary $Ge_{0.6}Sn_{0.1}Pb_{0.3}Te$ compound. *Scr. Mater.*, **62** (2), 89–92.

32 Gelbstein, Y., Rosenberg, Y., Sadia, Y., and Dariel, M.P. (2010) Thermoelectric properties evolution of spark plasma sintered $(Ge_{0.6}Pb_{0.3}Sn_{0.1})Te$ following a spinodal decomposition. *J. Phys. Chem. C*, **114**, 13126–13131.

33 Gelbstein, Y. (2012) Morphological effects on the electronic transport properties of three-phase thermoelectric materials. *J. Appl. Phys.*, **112**, 113721.